

Evaluation of ShARP Passive Rainfall Retrievals over Snow-Covered Land Surfaces and Coastal Zones

ARDESHIR M. EBTEHAJ

Utah Water Research Laboratory, Department of Civil and Environmental Engineering, Utah State University, Logan, Utah

RAFAEL L. BRAS

School of Civil and Environmental Engineering, Georgia Institute of Technology, Atlanta, Georgia

EFI FOUFOULA-GEORGIU

Department of Civil, Environmental and Geo-Engineering, University of Minnesota Twin Cities, Minneapolis, Minnesota

(Manuscript received 22 August 2015, in final form 3 January 2016)

ABSTRACT

Using satellite measurements in microwave bands to retrieve precipitation over land requires proper discrimination of the weak rainfall signals from strong and highly variable background Earth surface emissions. Traditionally, land retrieval methods rely on a weak signal of rainfall scattering on high-frequency channels and make use of empirical thresholding and regression-based techniques. Because of the increased surface signal interference, retrievals over radiometrically complex land surfaces—snow-covered lands, deserts, and coastal areas—are particularly challenging for this class of retrieval techniques. This paper evaluates the results by the recently proposed Shrunken Locally Linear Embedding Algorithm for Retrieval of Precipitation (ShARP) using data from the Tropical Rainfall Measuring Mission (TRMM) satellite. The study focuses on a radiometrically complex region, partly covering the Tibetan highlands, Himalayas, and Ganges–Brahmaputra–Meghna River basins, which is unique in terms of its diverse land surface radiation regime and precipitation type, within the TRMM domain. Promising results are presented using ShARP over snow-covered land surfaces and in the vicinity of coastlines, in comparison with the land rainfall retrievals of the standard TRMM 2A12, version 7, product. The results show that ShARP can significantly reduce the rainfall overestimation due to the background snow contamination and markedly improve detection and retrieval of rainfall in the vicinity of coastlines. During the calendar year 2013, compared to TRMM 2A25, it is demonstrated that over the study domain the root-mean-square difference can be reduced up to 38% annually, while the improvement can reach up to 70% during the cold months of the year.

1. Introduction

Accurate estimation of rainfall from space is of paramount importance for hydrologic and land–atmosphere studies, especially where ground measurements are not readily available. The launch of the Tropical Rainfall Measuring Mission (TRMM) satellite set a benchmark for

spaceborne estimation of rainfall over the tropics (40°S–40°N), providing an invaluable set of rainfall observations over 17 years with unprecedented accuracy and coverage. The recently launched Global Precipitation Measurement (GPM) core satellite, together with a constellation of partner satellites, will provide considerably extended spatial coverage of precipitation over higher latitudes (68°S–68°N). The TRMM satellite carried the TRMM Microwave Imager (TMI), which was an orthogonally polarized radiometer with nine channels centered on frequencies ranging from 10.7 to 85.5 GHz (Kummerow et al. 1998) with a swath width of 878 km (after 2001, during the postboost era). The GPM Microwave Imager

Corresponding author address: Ardeshir M. Ebtehaj, Utah Water Research Laboratory, Department of Civil and Environmental Engineering, Utah State University, 1600 Canyon Rd., Logan, UT 84321.
E-mail: m.ebtehaj@usu.edu

(GMI) provides 13 dual-polarized channels with central frequencies within 10.65–183.3 GHz over a swath width of 904 km, which provides more detailed information about the frozen hydrometeors (Hou et al. 2014) than its predecessor. On board both of these satellites are radars providing high-resolution measurements of precipitation reflectivity within a narrower swath width, concurrent with the radiometric measurements. The TRMM Precipitation Radar (PR) was a single-frequency Ku-band radar (13 GHz) with a 247-km swath width (during the postboost era), while the GPM carries a dual-frequency precipitation radar (DPR) operating at Ku and Ka bands (13 and 35 GHz) with a swath width of 245 and 120 km, respectively.

In the microwave frequency bands ranging from 1 to 200 GHz, it is well understood that the transparent window channels contain a mixture of surface and precipitation spectral signatures in the upwelling radiative fluxes reaching the top of the atmosphere (TOA; Grody 1988). Over the oceans, rainfall emission can be discriminated well from the radiometrically uniform, cold, and polarized background emission. This signature can be properly explained via the absorption–emission laws of the atmospheric radiative transfer, giving rise to well-developed physically based algorithms for rainfall retrieval over oceans (e.g., Wilheit et al. 1977, 1991; Berg and Chase 1992; Chang et al. 1999; Olson 1989; Mugnai et al. 1993; Kummerow and Giglio 1994a,b; Smith et al. 1994; Petty 1994a,b; Bauer et al. 2001; Kummerow et al. 1996, 2001, 2011). Among these, the so-called Bayesian algorithms have provided a viable path for operational rainfall retrievals. This family of algorithms relies on a priori collected, statistically representative databases that contain hydrometer profiles and their measured or simulated spectral radiances at TOA. Given the observed spectral radiance at TOA, candidate spectral radiances are found in the database, and then their corresponding rainfall profiles are used to estimate/retrieve precipitation values of interest. The algorithms by Wilheit et al. (1991) and Kummerow et al. (2001) have been successfully deployed for operational ocean retrieval of the Advanced Microwave Scanning Radiometer for Earth Observing System (AMSR-E) on board the *Aqua* satellite and TMI. Conversely, over land, radiometrically warm background emission typically masks the microwave rainfall emission signal, causing the retrieval algorithms to often hinge upon weak rainfall scattering on high-frequency channels. It turns out that, as the wavelength approaches the particle size, the scattering due to the large raindrops and/or ice crystals causes depression in the field of brightness temperatures (Tb) at high-frequency channels (e.g., 85 GHz). Traditionally, the radiometrically cold raining areas are

discerned from the nonraining background via a fixed thresholding scheme and then related to the surface rainfall through empirical regression-based equations. Among these are the seminal 85-GHz scattering index (SI) by Grody (1991) used for the SSM/I and the AMSR-E sensors (see also Ferraro et al. 1994; Ferraro and Marks 1995; Wilheit et al. 2003) and the $SI = Tb_{22v} - Tb_{85v}$ (where 22v and 85v refer to the 22 GHz and 85 GHz vertically polarized channels, respectively) used for the operational TMI 2A12 product (Kummerow et al. 2001; Gopalan et al. 2010). A thorough review of the SI methods can be found in Seto et al. (2005).

Specifically, the TMI land retrieval algorithm makes use of the scattering index greater than a certain threshold (e.g., 8 K) to discriminate the rainfall signal from the nonraining background, as the water vapor channel of 22 GHz is not very sensitive to the precipitation scattering. Although the scattering-based approaches have been the cornerstone of overland microwave rainfall retrievals, they often suffer from some well-known drawbacks (see Petty and Li 2013a) including the following:

- 1) The SI-based screening naturally cannot properly detect warm precipitation regimes lacking the scattering effects of ice crystals (Liu and Zipser 2009).
- 2) This technique often confuses the high-frequency depressions over snow-covered lands or deserts with those caused by ice/rainfall scattering and produces biased rainfall estimates.
- 3) Because of the underlying complexity and transient structure of the background radiation regime, this class of methods often misses light rainfall in the vicinity of coastlines.

In the GPM era, these drawbacks are of great importance, especially for hydrologic applications in temperate and cold climate regimes with complex land surface radiation dynamics.

It turns out that microwave emission signals in the frequency range 1–37 GHz respond well to the heterogeneity of the land surface features—for example, soil texture, roughness, and moisture content; vegetation density, pattern, and water content; and snow cover and water equivalent—while also containing partial information about the atmospheric constituents. For bare to sparsely vegetated land, soil layers with higher moisture content are less emissive and more polarized in low frequencies, especially in 1–37 GHz (Njoku and Entekhabi 1996; Njoku and Li 1999). Vegetation and rough surfaces often reduce the polarization signature because of their Lambertian-like reflection properties and are typically more emissive than their bare soil counterparts. Desert surfaces contain little moisture and exhibit large diurnal variability and polarization in their

thermal emission, especially for high frequencies with small penetration depth. Moreover, desert surfaces scatter the upwelling radiation in a manner very similar to light precipitation (Grody and Weng 2008). Owing to the snow metamorphism, snow emissivity exhibits markedly varying dynamics as a function of snow grain size, density, depth, water content, and ice crust effects (Grody 2008). Typically, snow emissivity sharply decreases from low- to high-microwave frequencies, especially for fresh snow, giving rise to appreciably cold radiometric temperatures in high-frequency channels (i.e., ≥ 37 GHz), very similar to the scattering signatures of ice crystals in raining clouds. This similarity often makes the retrieval problem notoriously ill posed. In other words, it is likely that nonraining and raining scenes with different atmospheric constituents exhibit similar scattering signals at TOA, especially over the aforementioned complex surfaces. This equifinality or nonuniqueness is naturally the main source of ambiguity for land rainfall retrievals, especially when the method only exploits the information content of a limited number of high-frequency channels. Hence, we need retrieval methods that can account for various interactions among different channels rather than only using a few high-frequency bands. In other words, all of the available spectral channels that contain partial information about the land surface emissivity and hydrometeor profile need to be exploited and properly encoded in a multispectral sense to improve rainfall retrieval over land by better constraining the solution of the retrieval problem. For instance, over snow-covered surfaces, the low-frequency channels (10–37 GHz) are radiometrically colder than their bare or vegetated counterpart surfaces (Grody 2008). Therefore, this piece of information needs to be properly accounted for to help decipher whether the depressions in high-frequency channels are due to the rainfall scattering or perhaps low emissivity of snow-covered land surfaces.

To this end, a growing body of research has been recently directed toward a better understanding of land surface emissivity dynamics for improving the rainfall retrieval over land (e.g., Skofronick-Jackson and Johnson 2011; Ferraro et al. 2013; Ringerud et al. 2014; Turk et al. 2014a,b). These efforts are of central importance in the GPM era, especially as the attempts are more toward Bayesian approaches for overland retrievals (see Kummerow et al. 2011; Munchak and Skofronick-Jackson 2013; Kummerow et al. 2015). Microwave land surface emissivity is typically estimated by purely physical modeling and/or radiative energy balance using satellite measurements. Physical modeling requires a land surface model (LSM) coupled with a Radiative Transfer Model (RTM) to capture the

space–time variability of both the structural and electromagnetic properties of the land surfaces. This family of methods (e.g., Ringerud et al. 2014) requires very detailed information about geophysical parameters controlling the land surface–atmosphere interactions, soil–vegetation dynamics, and their interactions with subsurface hydrologic processes. The availability of such parameters is often limited at a global scale (Prigent et al. 2006), especially at the fine space–time resolution of interest for rainfall retrieval. Energy balance approaches typically make use of satellite measurements of spectral brightness temperatures and estimates of the surface skin and atmospheric temperature–moisture profiles. These estimates are typically used to close the radiation budget at TOA to approximate the “clear sky” emissivity values (e.g., Prigent et al. 1997, 2006; Moncet et al. 2011; Norouzi et al. 2011), which may be used to improve rainfall retrieval over land (see Turk et al. 2014a,b).

In this paper, we do not attempt to directly estimate the land surface spectral emissivity and explicitly incorporate it in the rainfall retrieval algorithm. Rather, we explore the idea of “implicitly” encoding the land surface information content across all available frequency channels, as part of the recently proposed Bayesian methodology, called Shrunken Locally Linear Embedding Algorithm for Retrieval of Precipitation (ShARP) by Ebtahaj et al. (2015), briefly reviewed in section 2. In essence, the a priori database in this Bayesian algorithm is properly organized in an algebraically tractable manner via two fat matrices, called “rainfall” and “spectral dictionaries.” The spectral dictionary contains a large collection of Tb measurements, while the rainfall dictionary encompasses their corresponding simulated or observed rainfall profiles. Given a pixel-level measurement of spectral Tb values, this algorithm relies on a nearest neighbor search that uses information content of all frequency channels to properly narrow down the retrieval problem to a few physically relevant spectral candidates and their rainfall profiles. In this step, our algorithm classifies the measured Tb values into raining and nonraining signatures via a simple probabilistic voting rule (detection step). Then for the raining Tb measurements, it exploits a modern regularized weighted least squares estimator to retrieve the rainfall values of interest (estimation step). Section 3 is devoted to presenting some promising rainfall retrievals over a region in South and Southeast Asia with diverse land surface conditions and precipitation regimes. This study area covers the Ganges–Brahmaputra–Meghna basin and its delta that encompass some important land surface features, including the Tibetan highlands, Himalayan range, Thar Desert, Hengduan Mountains, and the Malabar coasts in the

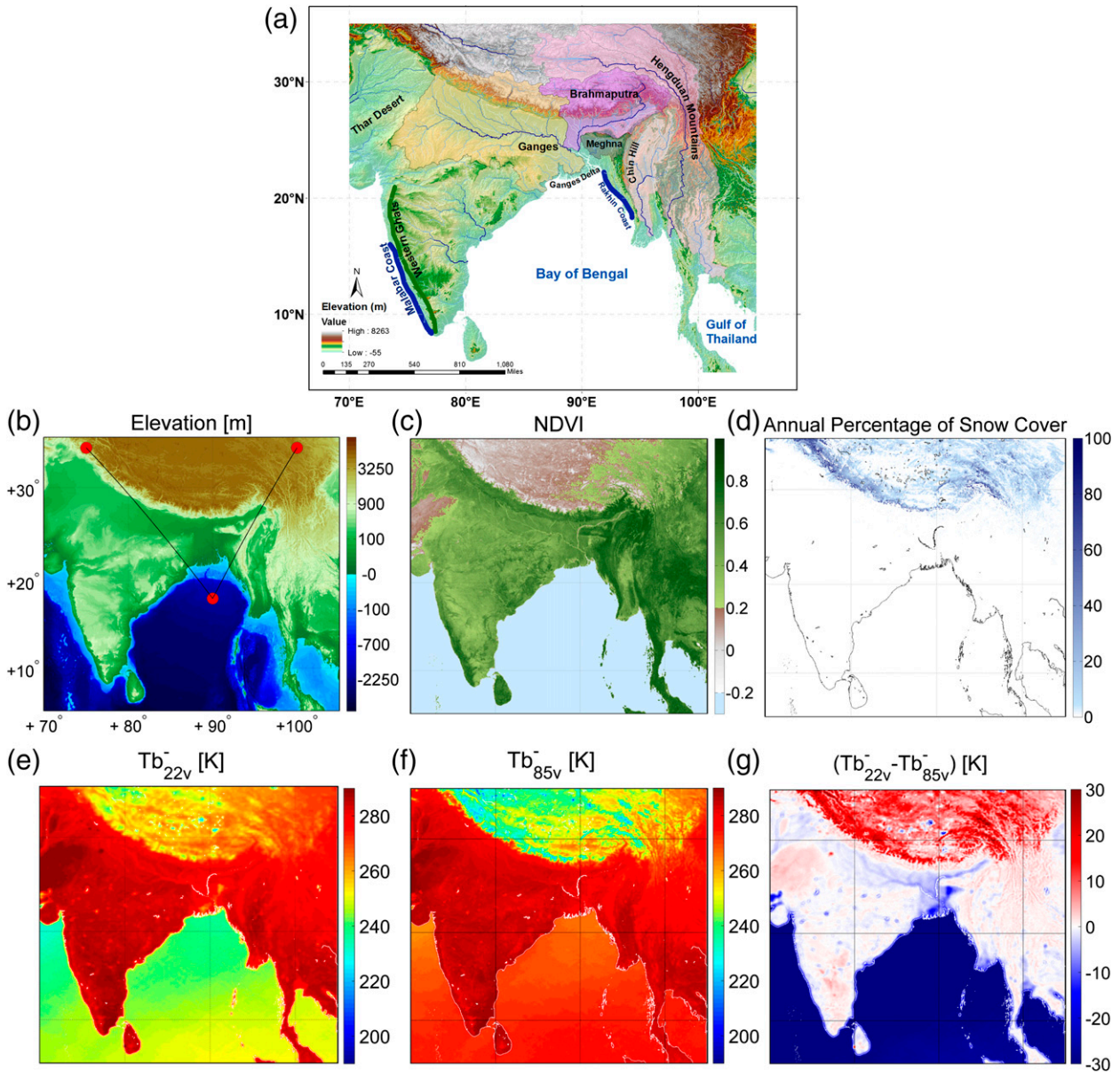


FIG. 1. (a) Geographic boundaries of the study region and some of its land surface characteristics. (b) Digital elevation model, (c) annual NDVI, and (d) percentage of snow-covered lands in 2013. The annual average of the rain-free scene brightness temperatures measured by the TMI sensor is shown for frequency channels (e) 22v, (f) 85v, and (g) their difference (i. e., $Tb_{22v}^- - Tb_{85v}^-$). For the tracks shown in (b), transects of all TMI channels, their corresponding NDVI, and snow percentage are shown in Fig. 2.

western Indian subcontinent (Fig. 1). Because of the snow-covered and frozen ground, especially over the Tibetan Plateau and Hengduan Mountains, this region has been notoriously problematic for the SI-based microwave retrievals (see Wang et al. 2009). Moreover, because of frequent inundation of the Ganges delta, dense irrigated agriculture, complex Earth surface dynamics of the river mouths, and presence of nearshore orographic features, this region is naturally a suitable test bed for examining the quality of rainfall retrievals over

wet surfaces and coastal zones. It is important to note that, although ShARP can be applied uniformly for retrievals both over ocean and land, in this paper, we confine our consideration only to its quantitative evaluation over land. To this end, we populate the spectral and rainfall dictionaries using collocated TMI 1B11 and PR 2A25 observations and compare the retrieval results with the standard TMI 2A12, version 7, operational land rainfall retrievals. We draw some concluding remarks and envision future research directions in section 4.

2. Retrieval methodologies

a. ShARP

In this subsection, we provide a brief explanation of ShARP for completeness, while a detailed account can be found in [Ebtehaj et al. \(2015\)](#). It is known that the passive rainfall retrieval in microwave bands can be defined as a mathematical inverse problem. In this inverse problem, we aim to obtain the rainfall profile (input) from the measured spectral brightness temperatures at TOA (output), while the Tb values can be related to the rainfall profile through the physical laws of radiative transfer. Let us assume that, at a pixel level, the observed spectral brightness temperatures at n_c channels are denoted by an n_c -element vector $\mathbf{y} = (y_1, y_2, \dots, y_{n_c})^T \in \mathfrak{R}^{n_c}$, while the rainfall profile of interest, sampled at n_r levels through the atmospheric depth, is $\mathbf{x} = (x_1, x_2, \dots, x_{n_r})^T \in \mathfrak{R}^{n_r}$. We can then assume that brightness temperatures are related to the rainfall profile via the following nonlinear mapping

$$\mathbf{y} = \mathcal{F}(\mathbf{x}) + \mathbf{v}, \quad (1)$$

where $\mathcal{F}: \mathbf{x} \rightarrow \mathbf{y}$ can be considered as a functional representation of a forward RTM and $\mathbf{v} \in \mathfrak{R}^{n_c}$ collectively represents the model/measurement error. As is evident, this mapping is extremely nonlinear, especially over land where the rainfall signal is severely masked by the background Earth emission. At the same time, as we only measure Tb values within a few spectral bands, different rainfall profiles may give rise to identical or very similar spectral brightness temperatures, making this inverse problem severely ill posed.

Let us assume that the a priori collected database is denoted by $\mathcal{D} = \{(\mathbf{b}_i, \mathbf{r}_i)\}_{i=1}^M$, where the curly brackets denote a set and where the pairs $\mathbf{b}_i = (b_{1i}, b_{2i}, \dots, b_{n_c i})^T \in \mathfrak{R}^{n_c}$ and $\mathbf{r}_i = (r_{1i}, r_{2i}, \dots, r_{n_r i})^T \in \mathfrak{R}^{n_r}$ are n_c - and n_r -element vectors representing pixel-level spectral brightness temperatures and their measured/simulated rainfall profiles. For notational convenience, we organize these pairs in two matrices $\mathbf{B} = [\mathbf{b}_1 | \dots | \mathbf{b}_M] \in \mathfrak{R}^{n_c \times M}$ and $\mathbf{R} = [\mathbf{r}_1 | \dots | \mathbf{r}_M] \in \mathfrak{R}^{n_r \times M}$, where the square brackets denote a matrix with column-wise concatenation of column vectors, called spectral and rainfall dictionaries, respectively.

Let us assume that $\mathbf{y} \in \mathfrak{R}^{n_c}$ denotes a pixel-level satellite measurement of the spectral brightness temperatures. In the first step, our algorithm isolates, in the Euclidean sense, a set \mathfrak{S} of ‘‘spectral neighbors’’ as the k -nearest neighbors of \mathbf{y} in the column space of \mathbf{B} . Then these spectral neighbors and their corresponding rainfall profiles in \mathbf{R} are stored in the pair of spectral $\mathbf{B}_{\mathfrak{S}} \in \mathfrak{R}^{n_c \times k}$ and rainfall $\mathbf{R}_{\mathfrak{S}} \in \mathfrak{R}^{n_r \times k}$ subdictionaries. In this step (detection step), we label \mathbf{y} as a raining or nonraining

pixel, using a simple classification rule. Specifically, we count the number of profiles in $\mathbf{R}_{\mathfrak{S}}$ that are raining at the surface. If the number of raining profiles is greater than or equal to pk , then we label \mathbf{y} as raining and attempt to estimate its rainfall profile. Note that, here, $p \in (0, 1]$ is a probability measure that controls the probability of hit and false alarm. In words, a smaller p value gives rise to larger probability of hit while a larger value reduces the probability of false alarm. We typically set $p = 0.5$, which corresponds to a majority vote rule for rain/no-rain classification. In the next step (estimation step), the algorithm attempts to approximate the observed raining spectral brightness temperatures, using a linear combination of the neighboring spectral candidates in $\mathbf{B}_{\mathfrak{S}}$ as follows:

$$\begin{aligned} & \underset{\mathbf{c}}{\text{minimize}} \quad \|\mathbf{W}^{1/2}(\mathbf{y} - \mathbf{B}_{\mathfrak{S}}\mathbf{c})\|_2^2 + \lambda_1 \|\mathbf{c}\|_1 + \lambda_2 \|\mathbf{c}\|_2^2 \\ & \text{subject to} \quad \mathbf{c} \geq 0, \mathbf{1}^T \mathbf{c} = 1, \end{aligned} \quad (2)$$

where ℓ_p -norm is $\|\mathbf{c}\|_p^p = \sum_i |c_i|^p$, $\mathbf{c} \geq 0$ denotes element-wise nonnegativity, λ_1 and λ_2 are positive regularization parameters, $\mathbf{W} \in \mathfrak{R}^{n_c \times n_c}$ is a positive definite precision matrix that determines the relative importance of each channel, and $\mathbf{1}^T = (1, \dots, 1)^T \in \mathfrak{R}^k$. This precision matrix encodes rainfall signal-to-noise ratio in each channel. For instance, it can be properly designed to give more weight to lower (e.g., 10 GHz) or higher frequencies (e.g., 85 GHz) while raining Tb measurements are over ocean or land, respectively. Note that the nonnegativity constraint is required to be physically consistent with the positivity of the Tb values in Kelvins, and the sum to unity constraint assures that the estimates are locally unbiased. Obtaining the representation coefficients $\hat{\mathbf{c}}$, by solving Eq. (2), the rainfall profile is then retrieved as $\hat{\mathbf{x}} = \mathbf{R}_{\mathfrak{S}}\hat{\mathbf{c}}$.

b. TMI 2A12 and differences with ShARP

As briefly noted, version 7 of the standard TMI 2A12 product uses a scattering index together with regression-based models for rainfall retrieval over land. However, over ocean, it makes use of an a priori collected database of rainfall–radiance pairs. In the following, for completeness, we briefly explain some basic details of the TMI 2A12 algorithm.

1) TMI 2A12: LAND RETRIEVAL

For each raining pixel, the algorithm interpolates between stratiform (strat) and convective (conv) rainfall mechanisms. To this end, it attempts to estimate a convective probability indicator p_c (see [McCollum and Ferraro 2003](#)) and then obtains an estimation of the near-surface rain rate as follows:

$$\hat{\mathbf{x}} = p_c \hat{\mathbf{x}}_{\text{conv}} + (1 - p_c) \hat{\mathbf{x}}_{\text{strat}}, \quad (3)$$

where $\hat{\mathbf{x}}_{\text{conv}}$ and $\hat{\mathbf{x}}_{\text{strat}}$ are rainfall estimates for convective and stratiform conditions as

$$\hat{\mathbf{x}}_{\text{conv}} = (-11.77 \times 10^{-6})\text{Tb}_{85v}^3 + (80.27 \times 10^{-4})\text{Tb}_{85v}^2 - 1.946\text{Tb}_{85v} + 182.68 \quad (4)$$

and

$$\hat{\mathbf{x}}_{\text{strat}} = (-70.8 \times 10^{-3})\text{Tb}_{85v} + 19.7. \quad (5)$$

The above regression equations are derived using collocated TMI–PR datasets explained in Liu et al. (2008). For a full exposition to the version 7 status of the land algorithm, one can refer to Gopalan et al. (2010).

2) TMI 2A12: OCEAN RETRIEVAL

Over oceans, TMI 2A12 relies on a Bayesian strategy. As noted by Kummerow et al. (2007), the expected value of rainfall profile of interest is obtained as follows:

$$\hat{\mathbf{x}} = \mathbb{E}(\mathbf{x}) = \frac{\sum_i \mathbf{r}_i \exp\{-0.5[\mathbf{y} - \mathcal{F}(\mathbf{r}_i)]^T \mathbf{V}^{-1}[\mathbf{y} - \mathcal{F}(\mathbf{r}_i)]\}}{\sum_i \exp\{-0.5[\mathbf{y} - \mathcal{F}(\mathbf{r}_i)]^T \mathbf{V}^{-1}[\mathbf{y} - \mathcal{F}(\mathbf{r}_i)]\}} \quad (6)$$

where \mathbf{V} is the covariance of model/observation error and $\{\mathbf{r}_i\}_{i=1}^M$ (where the curly brackets indicate a set of vectors) denotes the derived M rainfall profiles from a set of existing cloud-resolving model (CRM) simulations for which the associated vector of brightness temperatures $\{\mathbf{b}_i\}_{i=1}^M$ are obtained through an RTM as $\mathbf{b}_i = \mathcal{F}(\mathbf{r}_i)$. The estimator in Eq. (6) uses the inverse distance Gaussian weighting function to linearly combine a subset of rainfall profiles in the database that are isolated based on the sea surface temperature (SST) and total precipitable water (TPW). These variables can be obtained from ancillary sources or the onboard radiometer. It is important to note that although the exponential function in the above estimator dies off quickly, it never goes to zero. As a result, all of the isolated rainfall profiles are linearly combined in this estimator. In version 7, the algorithm uses a CRM-generated database that is made consistent with the TRMM PR observations as well (Kummerow et al. 2011).

ShARP uses a unified Bayesian approach over land and ocean and shares some similarities with GPROF, while exhibiting notable distinctions. Indeed, ShARP has its heritage in GPROF over ocean, in the sense that it obtains some optimal representation coefficients in the spectral space and then uses them to combine their corresponding rainfall profiles. However, there are several important technical distinctions between the two algorithms. Most notably, ShARP is a two-step algorithm

that first detects and then estimates the rainfall profile. The detection step in ShARP allows us to control the probability of detection and false alarm important for overland retrievals. More importantly, this step screens out physically irrelevant candidates and provides regionalization skills, which can make the rainfall retrievals robust to the underlying variability of the land surface emissivity. GPROF uses an inverse distance Gaussian weighting interpolation scheme (see Olson et al. 1996), which does not directly consider any prior probability for the used rainfall profiles [see Eq. (3) in Kummerow et al. (2007)]. However, ShARP relies on a modern variational method in Eq. (2), which can be interpreted as a Bayesian maximum a posteriori (MAP) estimator (Ebtehaj et al. 2015). This estimator obtains the coefficients in a weighted least squares sense and promotes sparsity in the solution by assigning nonzero coefficients only to a few relevant spectral neighbors, which can lead to improved recovery of high-intensity rainfall and prevent overly smooth retrievals. Moreover, because of the variational nature of this estimator, this framework can be easily extended for optimal integration of multiple sets of databases, models, and measurements across different instruments.

3. Results

To create the ShARP dictionaries, one may use the results of physical modeling, analogous to GPROF over the oceans, or just focus on satellite observations (e.g., TMI and PR) as presented in many previous efforts (e.g., Grecu and Anagnostou 2002; Skofronick-Jackson et al. 2003; Grecu et al. 2004; Petty and Li 2013a,b). In this paper, we focus on demonstrating the advantages of ShARP over land and use the collocated TMI 1B11, version 7, products and surface PR 2A25 to populate the dictionaries.

a. Study area

The study region (Fig. 1) is confined between 5° and 35°N latitude and 70° and 105°E longitude, extending from the Indus River basin and Thar Desert along the border of Pakistan and India to the Hengduan Mountains in southwestern China and Rakhine State in western Myanmar. From north to south, the region covers from the Tibetan highlands to the northern coastlines of the Bay of Bengal. This region is unique in terms of its diverse climate regimes, biodiversity, landforms, precipitation patterns, and types. In the northwest, the region contains the arid Thar Desert, while in the southwest it covers the coastlines of the Indian Peninsula, with a tropical wet climate influenced by the Western Ghats orographic features. In the north, the

elevated Tibetan Plateau in high altitudes has a cold arid steppe climate. The plateau is a glacier landform with a large number of brackish isolated lakes and is often covered with snow in cold seasons, especially in the vicinity of the Himalayan foothills. The Himalayan range sharply divides the cold upstream climate from the temperate climate of downstream lowlands at the base and has permanent snowpack in high elevations. It is important to note that the study area encompasses the Ganges–Brahmaputra–Meghna River basins, which drains more than 1.7 million km² from the Himalayas' headwaters to the Ganges delta (Frenken 2012). While the major areas of the basins are of temperate climate, the Meghna River basin in Bangladesh is of tropical climate and is among the wettest regions in the world, with annual precipitation that often exceeds 4000 mm (Mirza et al. 1998). The Ganges basin is heavily populated by dense irrigated agriculture, especially in the vicinity of its tributary. Rainfall in the study region is mainly controlled by the monsoon season from June to September. The Himalayan range typically forces the southwesterly moist monsoon winds to dump their moisture over the lowlands and shorelines of the region, while it leaves the Tibetan Plateau and Thar Desert relatively dry in rain shadows. The deltaic region often experiences very strong cyclonic storms during the monsoon season, some of which resulted in significant loss of life and properties. Among these was Cyclone Sidr, hitting the coastlines of Bangladesh in November 2007.

b. Surface condition and radiation regime

Figures 1a–d show the boundary and important geographic features of the study domain, digital elevation model, the annual normalized difference vegetation index (NDVI), and snow cover percentage in calendar year 2013. The vegetation and snow cover data are derived by averaging over the level 3 global monthly gridded products at 0.05° (MYD13C2 and MYD10CM), obtained from the Moderate Resolution Imaging Spectroradiometer (MODIS) instrument on board NASA's *Aqua* satellite. Figures 1e–g also show the annual fields of TMI brightness temperatures for the same year at 22v and 85v and their differences. Note that these T_b fields are obtained for precipitation-free scenes by overlying and averaging all overpasses of TMI within the inner swath, where the PR 2A25 is used for eliminating the raining areas.

Important radiation patterns can be seen, especially over snow-covered lands, wet surfaces, and in the vicinity of coastlines. In particular, even though among low-frequency channels the 22v exhibits a minimal response to the surface snow emissivity, we still see notable

depressions in this channel because of the presence of snow on the ground. More importantly, we see in Fig. 1g that the high-frequency depressions ($SI = T_{b22v} - T_{b85v}$) in rain-free scenes go beyond the prescribed ~ 8 K, especially over the headwaters of the Brahmaputra basin and the Hengduan Mountains. This observation suggests that the SI method is prone to false rainfall detection and may give rise to the rainfall overestimation above snow-covered lands. Near the coastlines, because of a marked difference between emissivity of ocean and land surfaces, we see a sharp temperature gradient at the interface, which poses challenges for rainfall retrieval.

To provide deeper insight into the information content of the low-frequency channels relevant to the rainfall retrieval problem, Fig. 2 shows one-dimensional transects of all frequency channels along the tracks shown in the digital elevation model in Fig. 1. On the one hand, below 28°N, the left track (track 1) passes mainly through moderately vegetated lowlands with $NDVI \approx 0.5$, while between 20° and 30°N, it crosses slightly denser vegetation with $NDVI = 0.6$ – 0.7 over the southward slope of the Himalayan range. Over higher latitudes this track records lower and highly variable $NDVI = 0.2$ – 0.6 and crosses land surfaces with at most 60% of annual snow cover. On the other hand, the right track (track 2) crosses the Chin Hills mountain range with tropical and subtropical forest ecosystem with high $NDVI$ values ranging mostly from 0.6 to 0.8 below latitude 27°N. For higher latitudes around 20°–30°N, this track goes over snow-covered and perhaps frozen grounds with $NDVI = 0.0$ – 0.4 , indicating the presence of sparse vegetation and steppe grasslands. In Fig. 2, over the tributaries of the Ganges River basin below 30°N latitude, track 1 exhibits large polarization and frequent radiometrically cold spots, especially for frequencies ≤ 37 GHz. For higher latitudes in this track, we see that the polarization gaps start to shrink over denser vegetation covers. It can be seen that the snow-covered surfaces create a sharp decrease in brightness temperatures and slightly increase polarization effects, especially for frequency channels ≥ 37 GHz. Note that while over vegetated areas, channel 85 GHz is typically warmer than 37 GHz; the presence of snow makes it cooler than 37 GHz. In track 2, we see less polarization compared to track 1 because of denser vegetation and rougher pathway over the Chin Hills. However, we see a few significant isolated drops in T_b values (see 10 and 37 h) due to the radiometrically cold wet surfaces, especially where the track crosses the Meghna–Brahmaputra River system and irrigated agricultural land surfaces. In this track, a significant temperature drop can be seen because of the high

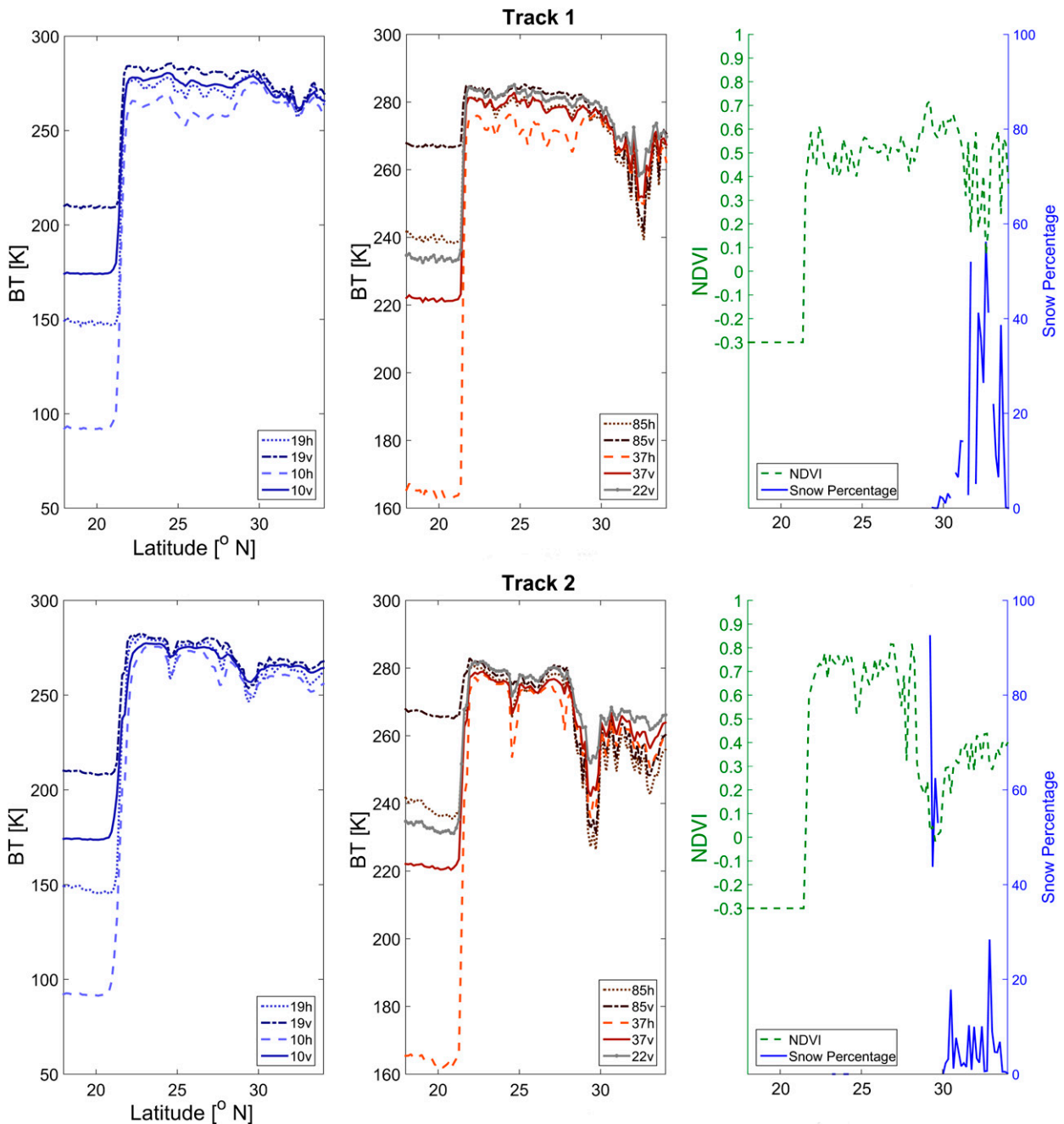


FIG. 2. One-dimensional transects of the nonraining TMI spectral Tb values, NDVI, and annual percentage of snow cover over the tracks shown in Fig. 1.

percentage of snow cover around 30°N in frequencies greater than 37 GHz.

The annual mean of the raining brightness temperatures along the first track is shown in Fig. 3. This transect of Tb values is analogous to those explained in Fig. 2, except for the scenes that are labeled as raining by the PR 2A25 data. The main goal is to demonstrate the

effect of the rainfall signal on high- and low-frequency channels and to provide some insights into how the nearest neighbor isolation of spectral candidates can provide partial regionalization skill to the ShARP retrievals. Over land, we clearly see that the rainfall spectral signals exhibit minimal influence on the low-frequency channels below 19 GHz, although some

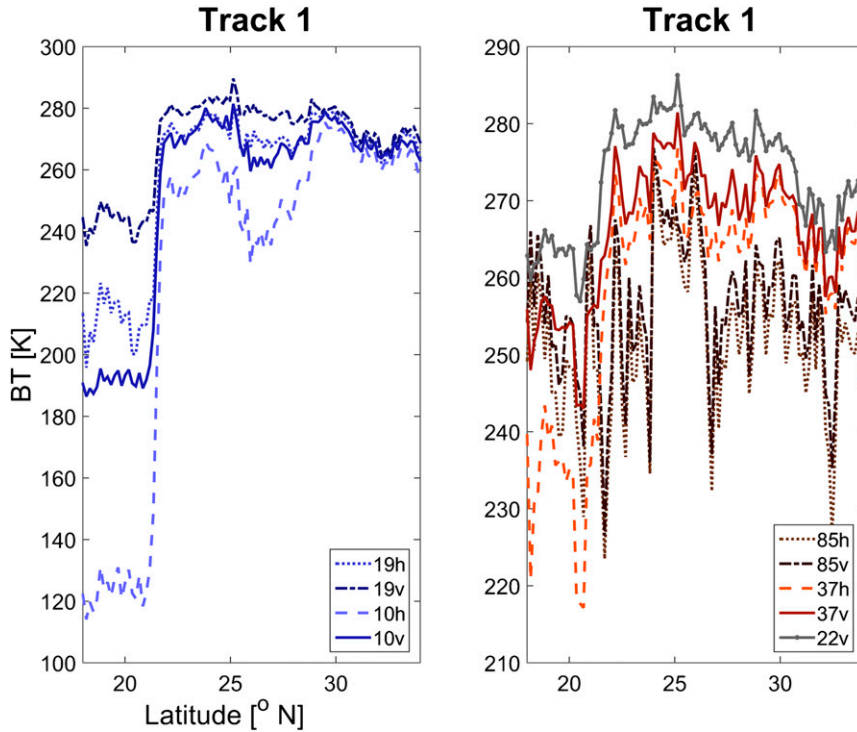


FIG. 3. One-dimensional transects of the raining TMI spectral Tb values over track 1 (see Fig. 1).

increased polarization can be seen compared to non-raining Tb values. However, the rainfall signatures are very pronounced over frequencies greater than 22 GHz and dramatically distort the background surface radiation pattern.

Let us assume that at each point of the i th track, here $i = \{1, 2\}$, the annual nonraining and raining Tb values are represented by $\mathbf{y}_i^- = (\text{Tb}_v^-)_{v \in \mathcal{V}}$ and $\mathbf{y}_i^+ = (\text{Tb}_v^+)_{v \in \mathcal{V}}$, respectively, where \mathcal{V} is the set of all available TMI channels. Furthermore, let us define the Euclidean distance

(dist) between nonraining and raining brightness temperatures along those tracks as $\text{dist}_{i,j} = \|\mathbf{y}_i^- - \mathbf{y}_j^+\|_2$, where $\|\mathbf{y}\|_2^2 = \sum_{v \in \mathcal{V}} \text{Tb}_v^2$. Figure 4 shows $\Delta_{\text{dist}1} = \text{dist}_{1,1} - \text{dist}_{1,2}$ (Fig. 4, left) and $\Delta_{\text{dist}2} = \text{dist}_{2,2} - \text{dist}_{2,1}$ (Fig. 4, right) for calendar year 2013. In words, for each track, this measure of distance difference characterizes the difference between the Euclidean distances of its non-raining background signal with the raining ones of both tracks. We see that the defined measure of distance difference falls below the x axis in almost 70% of the

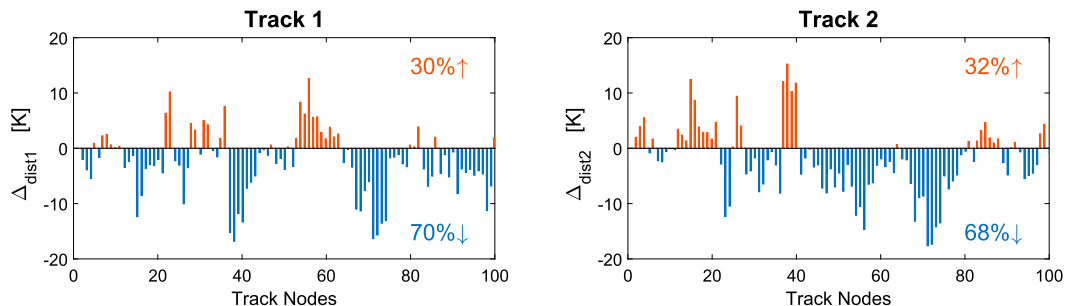


FIG. 4. Difference in Euclidean distance between the annual nonraining brightness temperatures along each track with the raining brightness temperatures along both tracks in calendar year 2013. The bars below the x axis show that in almost 70% of the points the raining brightness temperatures are closer to their nonraining counterparts along the same track. (left) Track 1 and (right) track 2 are shown in Fig. 1.

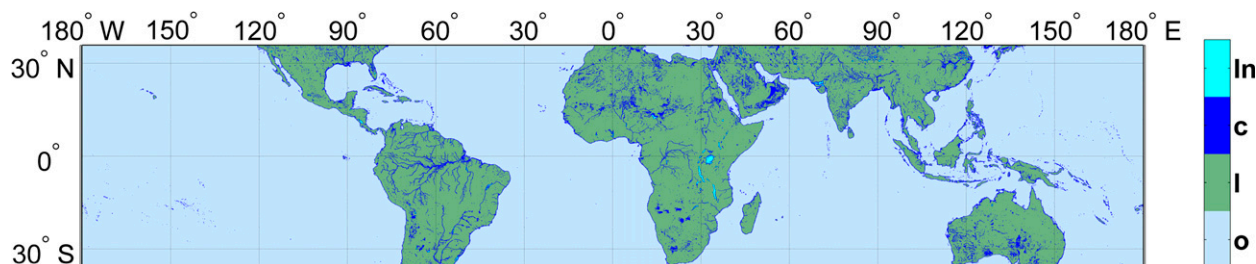


FIG. 5. ShARP land surface classes include inland water body (In), coastal zone (c), land (l), and ocean (o). The data are obtained from PR 1C21 product (version 7), mapped onto a regular grid at 0.05° (from Ebtehaj et al. 2015).

points in both tracks. In effect, in 70% of cases the raining points along each track are closer to their nonraining counterparts along the same track, which partly represent the underlying surface properties. In other words, it is likely that the surface properties of the nearest spectral neighbors are consistent with the surface properties under the retrieval scene, an important characteristic that needs to be taken into account in modern land retrieval techniques (see Turk et al. 2014a). By visual inspection and comparison of Figs. 2 and 3, we can see that this skill mainly comes from the low-frequency channels (10–19 GHz), for which the observed brightness temperatures mainly respond to the land surface emission and remain almost insensitive to the atmospheric signals. Thus, one might interpret this observation as a regionalization skill of the nearest neighbors isolation of the spectral candidates in ShARP.

c. ShARP parameterizations and settings

In this study we run ShARP for four different Earth surface classes, namely, ocean, land, coast, and inland water bodies (see Fig. 5). In other words, we collect four dictionaries and run the algorithm over each surface class depending on the geolocation of each pixel. This surface stratification is obtained from standard surface data in the PR 1C21, version 7, product in a $5\text{ km} \times 5\text{ km}$ grid box. To construct spectral and rainfall dictionaries, we used collocated pixels of TMI and PR in 2000 orbits, randomly chosen from a rainfall database collected in five years, 2002, 2005, 2008, 2011, and 2012. Note that the sampling was not confined to the study region and covers the entire TRMM domain. In these sampled orbits, more than 25 million raining and nonraining pixels were used to construct the required dictionaries. To obtain collocated radar radiometer data, we focused on the swath-level calibrated Tb values and near-surface rainfall in the TMI 1B11 and PR 2A25 (Iguchi et al. 2000) products, respectively. To this end, we mapped the TMI measurements onto the PR grids using the nearest neighbor interpolation.

In the detection step, we used $k = 50$ and found that the probabilities of hit and false alarm are not very sensitive to the number of nearest neighbors $k \geq 25$. Notice that in the detection step, we consider the information content of each channel equally important for the nearest neighbors search. However, in the estimation step, we use the precision matrix \mathbf{W} in Eq. (2) to properly encode the relative importance of each channel for rainfall estimation. For instance, we assign larger precision weights to low-frequency channels (e.g., 10 GHz) for retrievals over ocean while high-frequency channels (e.g., 85 GHz) receive larger weights over land. To this end, we used a diagonal precision matrix for which the nonzero elements are filled with the coefficients of variation of raining Tb values in each channel, obtained from the collected dictionaries (see Ebtehaj et al. 2015).

d. Instantaneous retrieval of the Cyclone Sidr

Cyclone Sidr was one of the most intense and historically disastrous tropical cyclones to hit the coastline of Bangladesh, on 15 November 2007. The TRMM satellite flew over the cyclone at 1359 UTC and provided critical information about the storm vertical structure and spatial extent. Figure 6 shows the retrieved rainfall rates obtained from ShARP and compares them with the standard version 7 of PR 2A25 and TMI 2A12.

We see that the multiband structure of the cyclone is retrieved well by ShARP (Fig. 6, right). Comparing the results with 2A25 (Fig. 6, middle) and 2A12 (Fig. 6, left), it is evident that the ShARP retrieval properly captures the high intense rainbands of the cyclone over land and in the vicinity of the coastline. For instance, the intense rainfall band—right above the Ganges delta—is estimated around 8 mm h^{-1} in the 2A12, while this estimate in both ShARP and 2A25 is around 16 mm h^{-1} . Furthermore, in the vicinity of the coastlines, we see some discontinuities over ocean in the 2A12 product. In these regions, it can be seen that some of the light rain patches close to the shoreline are underestimated or completely missed. However, the ShARP retrievals

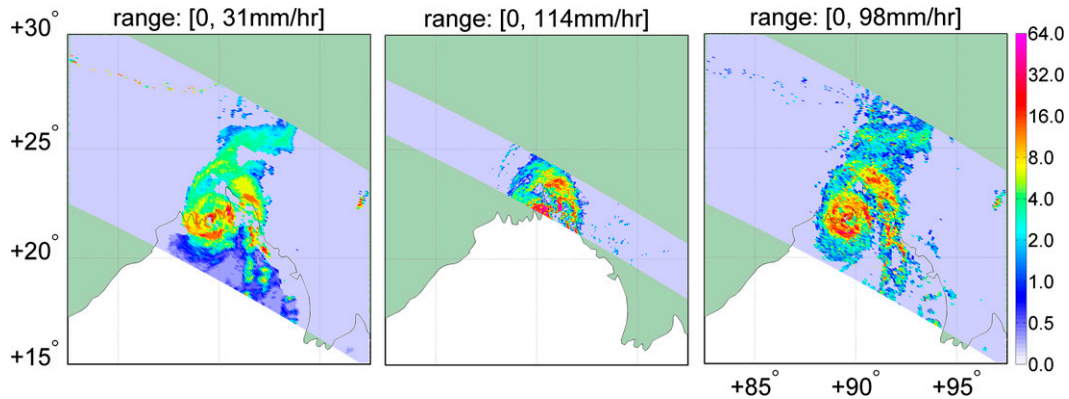


FIG. 6. Rainfall retrievals for the TRMM overpass capturing Cyclone Sidr at 1359 UTC 15 Nov 2007 from (left) 2A12, (middle) 2A25, and (right) ShARP.

remain relatively coherent close to the shoreline and some isolated rainfall patches are also recovered.

Given that an absolute reference rainfall field for the above snapshot is lacking, the objective comparison of these retrievals is not straightforward, especially over the ocean, where the databases are of different nature (i.e., observational for ShARP and mainly model based for 2A12). However, Fig. 7 compares the histogram and empirical cumulative distribution function (CDF) of the retrieved rainfall over the inner swath, which mostly captures the rainfall over land and in the vicinity of shorelines, where both algorithms attempt to reproduce the PR 2A25 rainfall. We clearly see that ShARP performs well in retrieving a wide range of rainfall intensities and properly resembles the distribution of rainfall provided by 2A25. It is seen that ShARP retrieves rainfall rates below 1 mm h^{-1} and above 14 mm h^{-1} , while a large probability mass of the retrieved rainfall remains between 2 and 5 mm h^{-1} in

2A12. The dynamic range of the retrieved rainfall is better illustrated in the CDF plots. Consistent with the shown histograms, we see that the passively retrieved rainfall values are mostly concentrated around the mode in 2A12 while the results in ShARP are stretched and properly resemble the reference 2A25 rainfalls. Obviously, both retrievals fall short to properly explain the thick tail distribution of the PR-retrieved rainfall; however, this problem seems to be ameliorated in ShARP.

The similarity of the rainfall histograms might be measured by the Kullback–Leibler (KL) divergence. The KL is a nonnegative measure that quantifies the closeness between a reference probability distribution $\mathcal{P} = \{p_i\}$ and an approximate one $\mathcal{P} = \{\hat{p}_i\}$ (where the curly brackets denote a set of probability measures),

$$KL(\mathcal{P}||\hat{\mathcal{P}}) = \sum_i p_i \log \frac{p_i}{\hat{p}_i}. \tag{7}$$

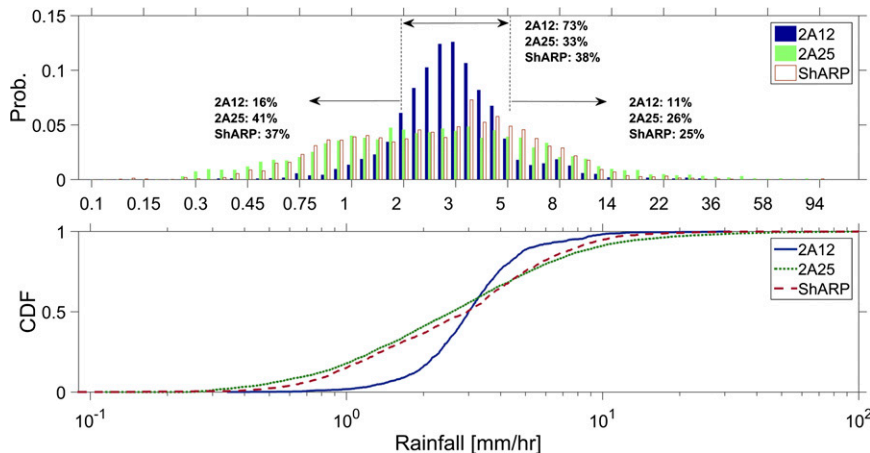


FIG. 7. (top) Pixel-level probability histograms and (bottom) empirical CDF of the retrieved rainfall over the inner swath of the TRMM overpass, capturing Cyclone Sidr at 1359 UTC 15 Nov 2007.

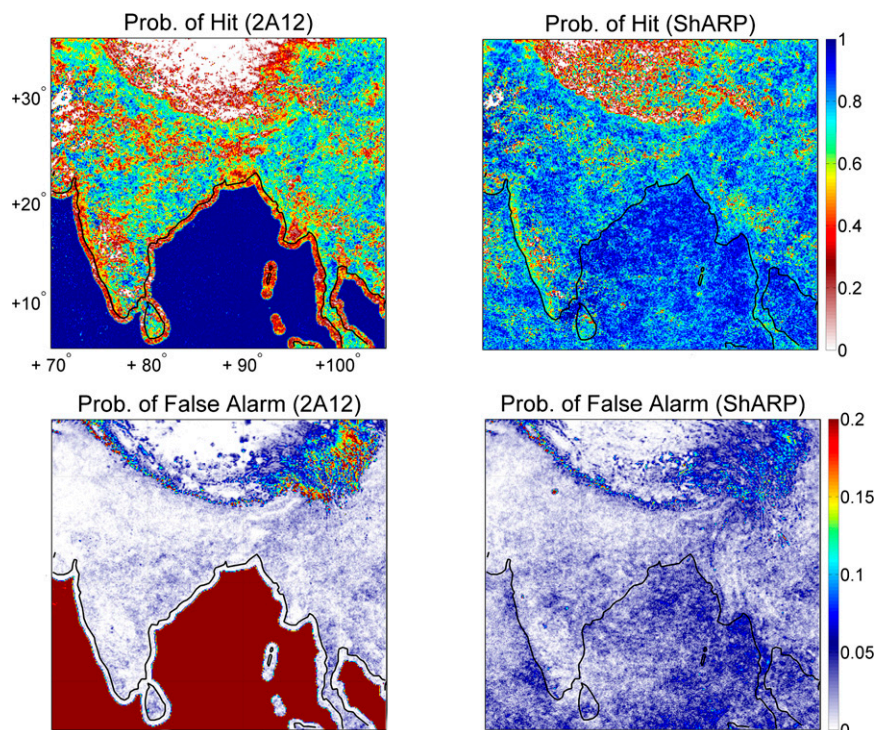


FIG. 8. Annual probability of hit and false alarm, comparing the 2A12 and ShARP retrievals with the 2A25 as a reference. The fields show probabilities obtained for all inner-swath overpasses in 2013 at 0.1° resolution.

As is evident, this measure is not symmetric and is zero when the distributions are identical. A simple calculation shows that the distribution of ShARP is much closer to the distribution of 2A25 than the 2A12 to 2A25, as an estimate of this measure reduces from 0.6 (2A12 vs 2A25) to 0.06 (ShARP vs 2A25).

e. Monthly and annual retrievals

To better quantify the quality of ShARP retrievals, we compare its monthly and annual retrievals with the standard 2A25 and 2A12 over the study domain in calendar year 2013. Even though we show the retrieval results both over ocean and land, we confine our interpretation only to the results over land and in the vicinity of coastlines, where both retrievals are empirical in their nature and attempt to reproduce the 2A25. We need to once again emphasize that 2A25 is not free of error; however, it provides one of the best estimates of the total rainfall at a global scale (see Berg et al. 2006).

To this end, we first focus on the detection capabilities of ShARP. Figure 8 shows maps of probabilities of hit and false alarm while the retrieval results of ShARP and 2A12 are compared binary-wise with 2A25 for all inner-swath overpasses in 2013. We can clearly see a few main points in ShARP retrievals: 1) coherent and improved

detection rate near the coastlines; 2) reduction of false alarm in rainfall detection over snow-covered land surfaces above the Himalayan range, headwaters of the Brahmaputra basin, and Hengduan Mountains (see Fig. 1); and 3) improved retrieval of the coastal orographic precipitation. We can observe that both 2A12 and ShARP are prone to detect fewer raining events than 2A25 near the coastlines (Fig. 8, top). We see a systematic decrease in the probability of detection over a strip of approximately 25–35 km parallel to the coastlines in 2A12, while the ShARP retrievals seem to robustly absorb the drastic emissivity transition at the land–ocean interface. In the vicinity of coastlines, the probability of hit mostly falls between 0.2 and 0.5 in 2A12, while it is within the range of 0.7–1.0 in ShARP. Over the Malabar Coast with tropical monsoon climate—between the Western Ghats mountain range and southwest coastlines of the Indian subcontinent—we also see that the probability of hit in both retrievals decreases appreciably. However, ShARP shows some improvements in this regime as well. Note that in this wet strip, the rainfall processes are mainly orographic and highly seasonal and their annual amount is mostly governed by the monsoon season from May to September. Therefore, we suspect that the decrease in probability of hit mostly

corresponds to the shallowness of the Western Ghats orographic lifting, which may give rise to weak ice signatures on high-frequency channels. The maps of the probability of false alarms (Fig. 8, bottom) reveal advantages of ShARP in retrieving rainfall over snow-covered lands. A notable decrease in the probability of false alarm over snow-covered surfaces in the Himalayan range and Hengduan Mountains is seen in ShARP retrievals. Over the tributaries of the Ganges river basin and its delta, with dense agricultural activities near the river banks and thus high soil moisture content, we observe improved probability of hit in ShARP. We also see that both methods show low detection skills in capturing sporadic and low-intensity rainfall over the dry region of the Tibetan Plateau. Specifically, the ShARP detection rate over the northern part of the plateau falls between 0.0 and 0.5, while this rate tends to zero in 2A12. However, we will demonstrate later on that these low values correspond to light rainfall amounts that may not exceed 5–20 mm yr⁻¹.

Figure 9 compares the seasonal retrievals of ShARP with the TRMM standard products. The objective is to further demonstrate the performance of ShARP retrievals close to the shorelines and over snow-covered mountainous regions. Figures 9a–d show 3-month rainfall (in millimeters) from January to December 2013. During the cold seasons such as January–March (JFM; Fig. 9a) and October–December (OND; Fig. 9d), we see considerable overestimation in passive retrievals along the Himalayan range and southeast of the plateau, covering the Hengduan Mountains. However, as is evident, this overestimation is markedly reduced in the ShARP retrievals. This improvement is largely due to the multispectral nature of ShARP and its nearest neighbors screening in the detection step. Indeed, as explained, information content of the lower-frequency channels allows us to better filter out the noisy background signal of snow and constrain the estimation step only to a few physically relevant candidates in the sub-dictionaries. It is worth noting that this improvement persists during the snow-melting season April–June (AMJ; Fig. 9b), indicating the robustness of our algorithm against the drastic changes in the temporal dynamics of snow emissivity.

During the warm months of the monsoon season in July–September (JAS; Fig. 9c), we see that both retrieval methods reproduce well the target 2A25 over the Tibetan highlands and the Himalayas. However, consistent with the observations in Fig. 8, some rainfall underestimation can be spotted over the coastal strip of the Malabar region in southeastern India and the Rakhine coasts in western Myanmar. The rainfall regime over both of these regions is heavily influenced by the

presence of the Western Ghats and Arakan orographic barriers blocking the moist southeasterly monsoon winds. Among these two coastal areas, it is important to note that the land–ocean interfacial radiation regime seems to be more complex at the vicinity of the Rakhine coastlines, particularly because of the presence of complex deltaic landforms and the dynamics of multiple river mouths. The observed underestimation in passive retrievals over the Malabar strip seems to be pronounced both over coasts and shores, perhaps indicating that the total rainfall is largely controlled by prolonged periods of warm and shallow orographic lifting. While less significant, underestimation over the coasts of the Rakhine State might be an indication that the rainfall is more influenced by deeper convections and more cold clouds in this region, compared with the Malabar strip.

Figure 10 shows some quantitative measures that compare monthly retrievals in 2013, restricted to land and coastal areas of the study domain. Specifically, we computed the monthly root-mean-square difference (RMSD) and mean absolute difference (MAD) of both retrievals with 2A25 and reported their relative reductions, for example, $(\text{RMSD}_{\text{ShARP}} - \text{RMSD}_{2\text{A}12})/\text{RMSD}_{2\text{A}12}$ (Fig. 10, left). As is evident, ShARP is markedly closer to 2A25 throughout the entire year, especially during cold seasons. The reduction in the chosen proximity metrics reaches up to 75% in the snow-falling months of November and December. As expected, the relative improvements of these metrics reach their minimum values (10%–15%) during the warm months of July–September, over which retrieval is less challenging for the SI-based techniques. We see notable differences between the reduction of RMSD and MAD metrics over the JFM period, which is apparently due to the precipitation overestimation above snow-covered land surfaces. Note that the RMSD quadratically penalizes the error and thus is more sensitive to large values and the tail of the distribution of retrieval differences than the MAD metric. The correlations (Fig. 10, right) of the monthly retrievals with 2A25 also confirm the observed trend in the evaluated proximity metrics. Indeed, we see that the quality of the monthly ShARP retrievals is robust and remains relatively independent of the seasonal rainfall variability and transition in land surface radiation regime.

Finally, density scatterplots of the retrieved annual rainfall are shown in Fig. 11. The results in this figure demonstrate pixel-level pairs of the annual rainfall estimates over land, in 2013, projected onto a regular grid at 0.2°. The density scatterplots confirm that both passive retrievals are slightly subject to underestimation of the high-intensity rainfall patches. We can also see that an

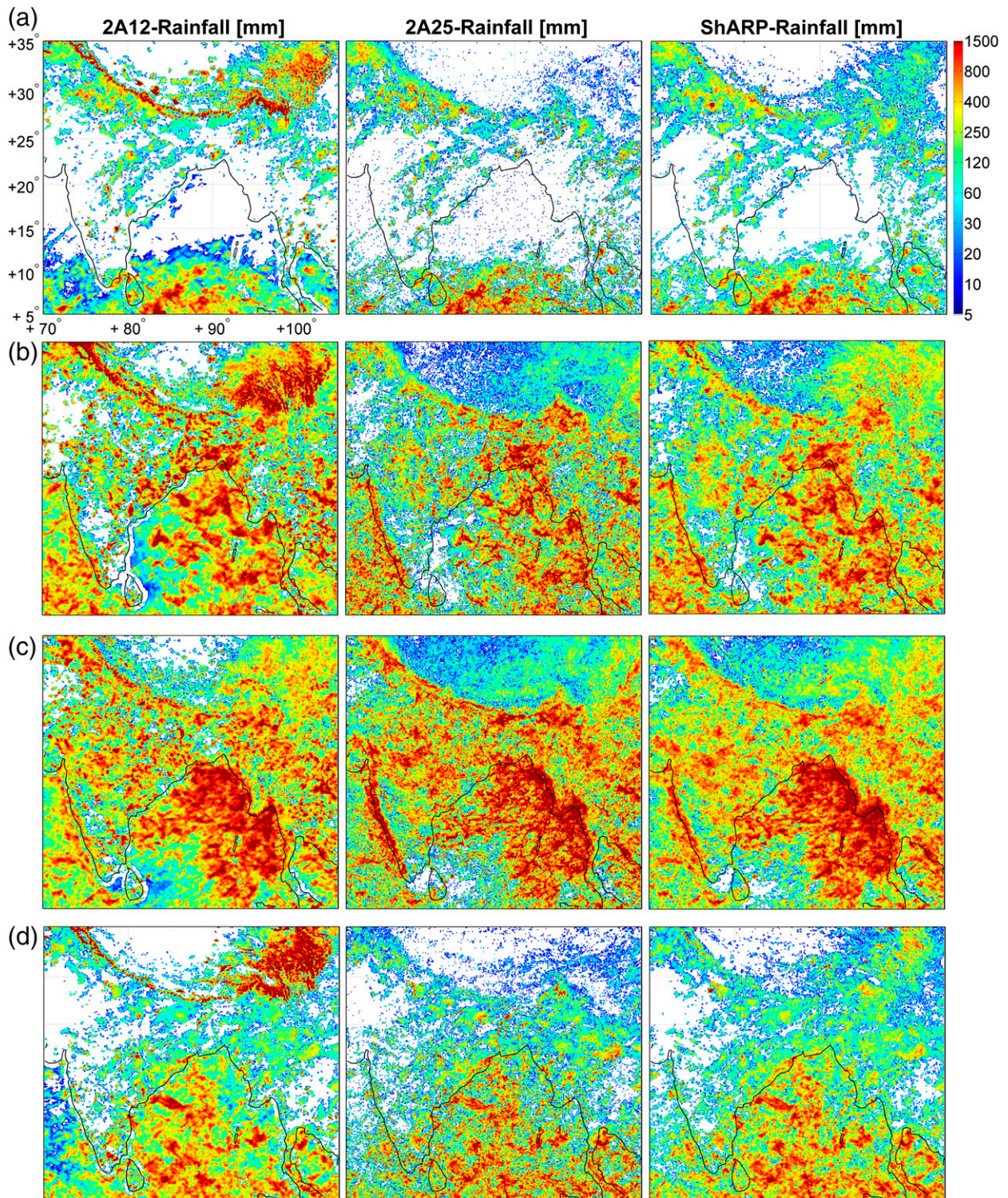


FIG. 9. Monthly rainfall retrievals over the study region shown at 0.1° . The 3-month accumulations of total rainfall (mm) are shown for (a) JFM, (b) AMJ, (c) JAS, and (d) OND throughout the calendar year 2013. The results only contain the rainfall captured within the TRMM inner swath.

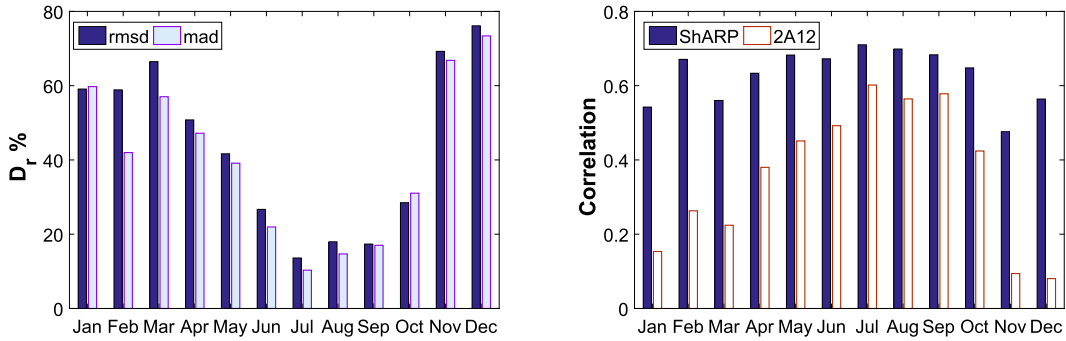


FIG. 10. (left) Relative reduction (%) in monthly RMSD and MAD in ShARP retrievals compared with 2A12. The results are confined to land and coastal areas of the study domain in 2013. The reference rainfall is set to be 2A25. (right) The correlation coefficients of the monthly retrieved fields with the 2A25.

appreciable amount of rainfall pairs are away from the 1:1 line in the 2A12, pointing to the notable overestimation reported in Fig. 9. Comparing annual passive retrievals with the 2A25, the annual RMSD in ShARP is 38% smaller than the one in the 2A12, mainly because of improved retrievals of rainfall over snow-covered ground. Note that, because of the reported overestimation, the annual correlation (corr) and coefficients of determination r^2 in 2A12 are less than 0.5, while these statistics reach 0.8 and 0.65 in ShARP, respectively.

4. Concluding remarks

We presented promising results for passive rainfall retrieval over land and coastal zones, using the recently proposed Shrunken Locally Linear Embedding Algorithm for Retrieval of Precipitation (ShARP; Ebtehaj et al. 2015). Even though the algorithm uses a single dictionary over land, the results indicate its robustness

to the underlying variability of land surface emissivity values. We provided evidence that as ShARP uses information across all spectral channels through a nearest neighbor detection step, it allows us to properly discriminate background radiation from the rainfall signal over snow-covered grounds. In the vicinity of coastlines, some improved results in rainfall detection and estimation are elucidated, which promise a step forward for applications related to snow and coastal hydrology in the era of the Global Precipitation Measuring (GPM) project. Research is currently underway to compare ShARP with ground-based observations and the results by the latest version of GPROF (Kummerow et al. 2015), which uses multiple surface classes to improve retrievals over land. While ShARP has been tested for observationally based TRMM data, its extension to use combined physically based and observationally generated dictionaries across multiple platform might be of future research interest.

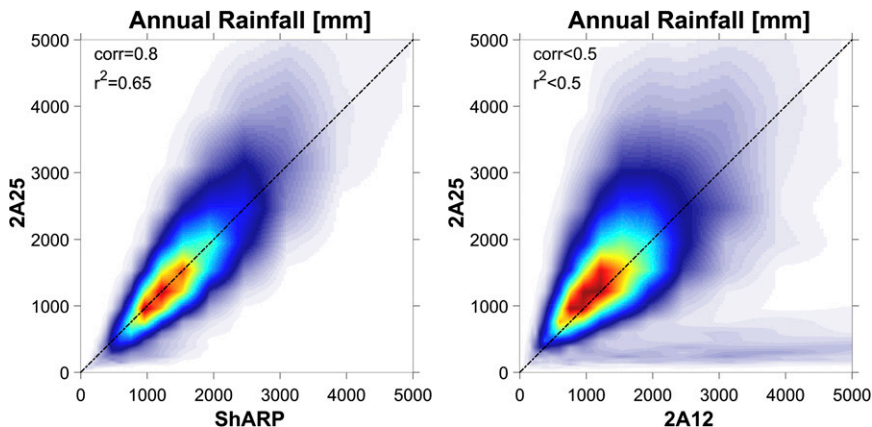


FIG. 11. Smooth scatterplots of the total rainfall (mm) for 2A25 vs (left) ShARP and (right) 2A12 in 2013. The plots are obtained from pairs of the total rainfall over land and coastal areas of the study domain projected onto a regular grid at 0.2° .

Acknowledgments. The first author would like to thank Professor Christian Kummerow and Dr. Dave Randel at Colorado State University for the provided insight and fruitful discussion through the course of this research. The authors also gratefully acknowledge the financial support provided by the K. Harrison Brown Family Chair; the Joseph T. and Rose S. Ling Chair; two NASA Global Precipitation Measurement Grants (NNX13AG33G and NNX13AH35G); and the USDA National Institute of Food and Agriculture, project 1008517, through the Agricultural Experiment Station at Utah State University. The TRMM 2A12 and 2A25 data were obtained through the anonymous File Transfer Protocol publicly available at <ftp://trmmopen.gsfc.nasa.gov/pub/trmmdata>. The MODIS retrievals (i.e., MYD13C2 and MYD10CM) were also obtained from the Land Processes Distributed Active Archive Center (LP DAAC), which are publicly accessible at https://lpdaac.usgs.gov/data_access/data_pool.

REFERENCES

- Bauer, P., P. Amayenc, C. D. Kummerow, and E. A. Smith, 2001: Over-ocean rainfall retrieval from multisensor data of the Tropical Rainfall Measuring Mission. Part II: Algorithm implementation. *J. Atmos. Oceanic Technol.*, **18**, 1838–1855, doi:10.1175/1520-0426(2001)018<1838:OORRFM>2.0.CO;2.
- Berg, W., and R. Chase, 1992: Determination of mean rainfall from the Special Sensor Microwave/Imager (SSM/I) using a mixed lognormal distribution. *J. Atmos. Oceanic Technol.*, **9**, 129–141, doi:10.1175/1520-0426(1992)009<0129:DOMRFT>2.0.CO;2.
- , T. L'Ecuyer, and C. Kummerow, 2006: Rainfall climate regimes: The relationship of regional TRMM rainfall biases to the environment. *J. Appl. Meteor. Climatol.*, **45**, 434–454, doi:10.1175/JAM2331.1.
- Chang, A. T. C., L. S. Chiu, C. Kummerow, J. Meng, and T. T. Wilheit, 1999: First results of the TRMM Microwave Imager (TMI) monthly oceanic rain rate: Comparison with SSM/I. *Geophys. Res. Lett.*, **26**, 2379–2382, doi:10.1029/1998GL900452.
- Ebtehaj, A. M., R. L. Bras, and E. Foufoula-Georgiou, 2015: Shrunk locally linear embedding for passive microwave retrieval of precipitation. *IEEE Trans. Geosci. Remote.*, **53**, 3720–3736, doi:10.1109/TGRS.2014.2382436.
- Ferraro, R. R., and G. F. Marks, 1995: The development of SSM/I rain-rate retrieval algorithms using ground-based radar measurements. *J. Atmos. Oceanic Technol.*, **12**, 755–770, doi:10.1175/1520-0426(1995)012<0755:TDSRR>2.0.CO;2.
- , N. C. Grody, and G. F. Marks, 1994: Effects of surface conditions on rain identification using the DMSP-SSM/I. *Remote Sens. Rev.*, **11**, 195–209, doi:10.1080/02757259409532265.
- , and Coauthors, 2013: An evaluation of microwave land surface emissivities over the continental United States to benefit GPM-era precipitation algorithms. *IEEE Trans. Geosci. Remote.*, **51**, 378–398, doi:10.1109/TGRS.2012.2199121.
- Frenken, K., 2012: Irrigation in southern and eastern Asia in figures: AQUASTAT Survey—2011. FAO Water Rep. 37, FAO Land and Water Division, 487 pp.
- Gopalan, K., N.-Y. Wang, R. Ferraro, and C. Liu, 2010: Status of the TRMM 2A12 land precipitation algorithm. *J. Atmos. Oceanic Technol.*, **27**, 1343–1354, doi:10.1175/2010JTECHA1454.1.
- Greco, M., and E. N. Anagnostou, 2002: Use of passive microwave observations in a radar rainfall-profiling algorithm. *J. Appl. Meteor.*, **41**, 702–715, doi:10.1175/1520-0450(2002)041<0702:UOPMOI>2.0.CO;2.
- , W. S. Olson, and E. N. Anagnostou, 2004: Retrieval of precipitation profiles from multiresolution, multifrequency active and passive microwave observations. *J. Appl. Meteor.*, **43**, 562–575, doi:10.1175/1520-0450(2004)043<0562:ROPPFM>2.0.CO;2.
- Grody, N., 1988: Surface identification using satellite microwave radiometers. *IEEE Trans. Geosci. Remote Sens.*, **26**, 850–859, doi:10.1109/36.7716.
- , 1991: Classification of snow cover and precipitation using the Special Sensor Microwave Imager. *J. Geophys. Res.*, **96**, 7423–7435, doi:10.1029/91JD00045.
- , 2008: Relationship between snow parameters and microwave satellite measurements: Theory compared with Advanced Microwave Sounding Unit observations from 23 to 150 GHz. *J. Geophys. Res.*, **113**, D22108, doi:10.1029/2007JD009685.
- , and F. Weng, 2008: Microwave emission and scattering from deserts: Theory compared with satellite measurements. *IEEE Trans. Geosci. Remote Sens.*, **46**, 361–375, doi:10.1109/TGRS.2007.909920.
- Hou, A. Y., and Coauthors, 2014: The Global Precipitation Measurement Mission. *Bull. Amer. Meteor. Soc.*, **95**, 701–722, doi:10.1175/BAMS-D-13-00164.1.
- Iguchi, T., T. Kozu, R. Meneghini, J. Awaka, and K. I. Okamoto, 2000: Rain-profiling algorithm for the TRMM Precipitation Radar. *J. Appl. Meteor.*, **39**, 2038–2052, doi:10.1175/1520-0450(2001)040<2038:RPAFTT>2.0.CO;2.
- Kummerow, C., and L. Giglio, 1994a: A passive microwave technique for estimating rainfall and vertical structure information from space. Part I: Algorithm description. *J. Appl. Meteor.*, **33**, 3–18, doi:10.1175/1520-0450(1994)033<0003:APMTFE>2.0.CO;2.
- , and —, 1994b: A passive microwave technique for estimating rainfall and vertical structure information from space. Part II: Applications to SSM/I data. *J. Appl. Meteor.*, **33**, 19–34, doi:10.1175/1520-0450(1994)033<0019:APMTFE>2.0.CO;2.
- , W. S. Olson, and L. Giglio, 1996: A simplified scheme for obtaining precipitation and vertical hydrometeor profiles from passive microwave sensors. *IEEE Trans. Geosci. Remote.*, **34**, 1213–1232, doi:10.1109/36.536538.
- , W. Barnes, T. Kozu, J. Shiue, and J. Simpson, 1998: The Tropical Rainfall Measuring Mission (TRMM) sensor package. *J. Atmos. Oceanic Technol.*, **15**, 809–817, doi:10.1175/1520-0426(1998)015<0809:TTRMMT>2.0.CO;2.
- , and Coauthors, 2001: The evolution of the Goddard Profiling Algorithm (GPROF) for rainfall estimation from passive microwave sensors. *J. Appl. Meteor.*, **40**, 1801–1820, doi:10.1175/1520-0450(2001)040<1801:TEOTGP>2.0.CO;2.
- , H. Masunaga, and P. Bauer, 2007: A next-generation microwave rainfall retrieval algorithm for use by TRMM and GPM. *Measuring Precipitation from Space*, V. Levizzani, P. Bauer, and F. Turk, Eds., Advances in Global Change Research, Vol. 28, Springer, 235–252, doi:10.1007/978-1-4020-5835-6_19.
- , S. Ringerud, J. Crook, D. Randel, and W. Berg, 2011: An observationally generated a priori database for microwave rainfall retrievals. *J. Atmos. Oceanic Technol.*, **28**, 113–130, doi:10.1175/2010JTECHA1468.1.
- , D. L. Randel, M. Kulie, N. Y. Wang, R. Ferraro, S. J. Munchak, and V. Petrovic, 2015: The evolution of the Goddard Profiling Algorithm to a fully parametric scheme. *J. Atmos. Oceanic Technol.*, **32**, 2265–2280, doi:10.1175/JTECH-D-15-0039.1.

- Liu, C., and E. J. Zipser, 2009: "Warm rain" in the tropics: Seasonal and regional distributions based on 9 yr of TRMM data. *J. Climate*, **22**, 767–779, doi:10.1175/2008JCLI2641.1.
- , —, D. J. Cecil, S. W. Nesbitt, and S. Sherwood, 2008: A cloud and precipitation feature database from nine years of TRMM observations. *J. Appl. Meteor. Climatol.*, **47**, 2712–2728, doi:10.1175/2008JAMC1890.1.
- McCollum, J. R., and R. R. Ferraro, 2003: Next generation of NOAA/NESDIS TMI, SSM/I, and AMSR-E microwave land rainfall algorithms. *J. Geophys. Res.*, **108**, 8382, doi:10.1029/2001JD001512.
- Mirza, M. Q., R. A. Warrick, N. J. Ericksen, and G. J. Kenny, 1998: Trends and persistence in precipitation in the Ganges, Brahmaputra and Meghna River basins. *Hydrol. Sci. J.*, **43**, 845–858, doi:10.1080/02626669809492182.
- Moncet, J.-L., P. Liang, J. F. Galantowicz, A. E. Lipton, G. Uymin, C. Prigent, and C. Grassotti, 2011: Land surface microwave emissivities derived from AMSR-E and MODIS measurements with advanced quality control. *J. Geophys. Res.*, **116**, D16104, doi:10.1029/2010JD015429.
- Mugnai, A., E. A. Smith, and G. J. Tripoli, 1993: Foundations for statistical-physical precipitation retrieval from passive microwave satellite measurements. Part II: Emission-source and generalized weighting-function properties of a time-dependent cloud-radiation model. *J. Appl. Meteor.*, **32**, 17–39, doi:10.1175/1520-0450(1993)032<0017:FFSPRF>2.0.CO;2.
- Munchak, S. J., and G. Skofronick-Jackson, 2013: Evaluation of precipitation detection over various surfaces from passive microwave imagers and sounders. *Atmos. Res.*, **131**, 81–94, doi:10.1016/j.atmosres.2012.10.011.
- Njoku, E. G., and D. Entekhabi, 1996: Passive microwave remote sensing of soil moisture. *J. Hydrol.*, **184**, 101–129, doi:10.1016/0022-1694(95)02970-2.
- , and L. Li, 1999: Retrieval of land surface parameters using passive microwave measurements at 6–18 GHz. *IEEE Trans. Geosci. Remote Sens.*, **37**, 79–93, doi:10.1109/36.739125.
- Norouzi, H., M. Temimi, W. B. Rossow, C. Pearl, M. Azarderakhsh, and R. Khanbilvardi, 2011: The sensitivity of land emissivity estimates from AMSR-E at C and X bands to surface properties. *Hydrol. Earth Syst. Sci.*, **15**, 3577–3589, doi:10.5194/hess-15-3577-2011.
- Olson, W. S., 1989: Physical retrieval of rainfall rates over the ocean by multispectral microwave radiometry: Application to tropical cyclones. *J. Geophys. Res.*, **94**, 2267–2280, doi:10.1029/JD094iD02p02267.
- , C. D. Kummerow, G. M. Heymsfield, and L. Giglio, 1996: A method for combined passive-active microwave retrievals of cloud and precipitation profiles. *J. Appl. Meteor.*, **35**, 1763–1789, doi:10.1175/1520-0450(1996)035<1763:AMFCPM>2.0.CO;2.
- Petty, G. W., 1994a: Physical retrievals of over-ocean rain rate from multichannel microwave imagery. Part I: Theoretical characteristics of normalized polarization and scattering indices. *Meteor. Atmos. Phys.*, **54**, 79–99, doi:10.1007/BF01030053.
- , 1994b: Physical retrievals of over-ocean rain rate from multichannel microwave imagery. Part II: Algorithm implementation. *Meteor. Atmos. Phys.*, **54**, 101–121, doi:10.1007/BF01030054.
- , and K. Li, 2013a: Improved passive microwave retrievals of rain rate over land and ocean. Part I: Algorithm description. *J. Atmos. Oceanic Technol.*, **30**, 2493–2508, doi:10.1175/JTECH-D-12-00144.1.
- , and —, 2013b: Improved passive microwave retrievals of rain rate over land and ocean. Part II: Validation and intercomparison. *J. Atmos. Oceanic Technol.*, **30**, 2509–2526, doi:10.1175/JTECH-D-12-00184.1.
- Prigent, C., W. B. Rossow, and E. Matthews, 1997: Microwave land surface emissivities estimated from SSM/I observations. *J. Geophys. Res.*, **102**, 21 867–21 890, doi:10.1029/97JD01360.
- , F. Aires, and W. B. Rossow, 2006: Land surface microwave emissivities over the globe for a decade. *Bull. Amer. Meteor. Soc.*, **87**, 1573–1584, doi:10.1175/BAMS-87-11-1573.
- Ringerud, S., C. Kummerow, C. Peters-Lidard, Y. Tian, and K. Harrison, 2014: A comparison of microwave window channel retrieved and forward-modeled emissivities over the U.S. Southern Great Plains. *IEEE Trans. Geosci. Remote Sens.*, **52**, 2395–2412, doi:10.1109/TGRS.2013.2260759.
- Seto, S., N. Takahashi, and T. Iguchi, 2005: Rain/no-rain classification methods for microwave radiometer observations over land using statistical information for brightness temperatures under no-rain conditions. *J. Appl. Meteor.*, **44**, 1243–1259, doi:10.1175/JAM2263.1.
- Skofronick-Jackson, G., and B. T. Johnson, 2011: Surface and atmospheric contributions to passive microwave brightness temperatures for falling snow events. *J. Geophys. Res.*, **116**, D02213, doi:10.1029/2010JD014438.
- , J. R. Wang, G. M. Heymsfield, R. Hood, W. Manning, R. Meneghini, and J. A. Weinman, 2003: Combined radiometer-radar microphysical profile estimations with emphasis on high-frequency brightness temperature observations. *J. Appl. Meteor.*, **42**, 476–487, doi:10.1175/1520-0450(2003)042<0476:CRRMPE>2.0.CO;2.
- Smith, E., X. Xiang, A. Mugnai, and G. Tripoli, 1994: Design of an inversion-based precipitation profile retrieval algorithm using an explicit cloud model for initial guess microphysics. *Meteor. Atmos. Phys.*, **54**, 53–78, doi:10.1007/BF01030052.
- Turk, F. J., Z. S. Haddad, and Y. You, 2014a: Principal components of multifrequency microwave land surface emissivities. Part I: Estimation under clear and precipitating conditions. *J. Hydrometeorol.*, **15**, 3–19, doi:10.1175/JHM-D-13-08.1.
- , L. Li, and Z. S. Haddad, 2014b: A physically based soil moisture and microwave emissivity data set for Global Precipitation Measurement (GPM) applications. *IEEE Trans. Geosci. Remote.*, **52**, 7637–7650, doi:10.1109/TGRS.2014.2315809.
- Wang, N.-Y., C. Liu, R. Ferraro, D. Wolff, E. Zipser, and C. Kummerow, 2009: TRMM 2A12 land precipitation product—Status and future plans. *J. Meteor. Soc. Japan.*, **87A**, 237–253, doi:10.2151/jmsj.87A.237.
- Wilheit, T. T., A. T. C. Chang, M. S. V. Rao, E. B. Rodgers, and J. S. Theon, 1977: A satellite technique for quantitatively mapping rainfall rates over the oceans. *J. Appl. Meteor.*, **16**, 551–560, doi:10.1175/1520-0450(1977)016<0551:ASTFQM>2.0.CO;2.
- , —, and L. S. Chiu, 1991: Retrieval of monthly rainfall indices from microwave radiometric measurements using probability distribution functions. *J. Atmos. Oceanic Technol.*, **8**, 118–136, doi:10.1175/1520-0426(1991)008<0118:ROMRIF>2.0.CO;2.
- , C. Kummerow, and R. Ferraro, 2003: Rainfall algorithms for AMSR-E. *IEEE Trans. Geosci. Remote Sens.*, **41**, 204–214, doi:10.1109/TGRS.2002.808312.